Elimination of an isolated pore: Effect of grain size

Wan Y. Shih
Department of Chemical Engineering and Princeton Materials Institute, Princeton University,
Princeton, New Jersey 08544-5263

Wei-Heng Shih
Department of Materials Engineering, Drexel University, Philadelphia, Pennsylvania 19104

Ilhan A. Aksay
Department of Chemical Engineering and Princeton Materials Institute, Princeton University,
Princeton, New Jersey 08544-5263

The effect of grain size on the elimination of an isolated pore was investigated both by the Monte Carlo simulations and by a scaling analysis. The Monte Carlo statistical mechanics model for sintering was constructed by mapping microstructures onto domains of vectors of different orientations as grains and domains of vacancies as pores. The most distinctive feature of the simulations is that we allow the vacancies to move. By incorporating the outer surfaces of the sample in the simulations, sintering takes place via vacancy diffusion from the pores to the outer sample surfaces. The simulations were performed in two dimensions. The results showed that the model is capable of displaying various sintering phenomena such as evaporation and condensation, rounding of a sharp corner, pore coalescence, thermal etching, neck formation, grain growth, and growth of large pores. For the elimination of an isolated pore, the most salient result is that the scaling law of the pore elimination time t_p with respect to the pore diameter d_p changes as pore size changes from larger than the grains to smaller than the grains. For example, in sample-size-fixed simulations, $t_p \sim d_p^3$ for $d_p < G$ and $t_p \sim d_p^2$ for $d_p > G$ with the crossover pore diameter d_c increasing linearly with G where G is the average grain diameter. For sample-size-scaled simulations, $t_p \sim d_p^4$ for $d_p < G$ and $t_p \sim d_p^3$ for $d_p > G$. That t_p has different scaling laws in different grain-size regimes is a result of grain boundaries serving as diffusion channels in a fine-grain microstructure such as those considered in the simulations. A scaling analysis is provided to explain the scaling relationships among t_p, d_p, and G obtained in the simulations. The scaling analysis also shows that these scaling relationships are independent of the dimensionality. Thus, the results of the two-dimensional simulations should also apply in three dimensions.

I. INTRODUCTION

Materials processing by sintering of powder compacts has been a central issue in the field of ceramics and metallurgy. With increasing emphasis on nanostructural design, an aspect of sintering that requires more adequate understanding is the densification of nanometer-sized particles without grain growth beyond 100 nm. This is the size range where the pores and the particles are of similar size and thus the spatial distribution of the porosity plays an increasingly significant role on the evolution of structure. In this size range, due to the formation of particle agglomerates, powder compacts often exhibit hierarchical pore-size distributions and thus while some pores are smaller than or equal to the particles, others are much larger than the particle size.[1] Individual particles can be polycrystalline as well,[2] adding to the complexity of the structure and the densification kinetics. With increasingly complicated structures, it is important to know how sintering is affected by the difference in the structures. For example, a different pore size/grain size ratio can affect the number of grain boundaries intersecting the pore surface. Theories that treated sintering as a diffusion-driven phenomenon have assumed that pores are surrounded by a certain number of grains and thus did not take into account the effect of a different pore size/grain size ratio explicitly. On the other hand, the pore stability argument of Kingery and Francois[4] that addressed the effect of pore size/grain size ratio did so only within the framework of thermodynamics and neglected the diffusional aspects.

In this paper, we study the role of structural features on sintering by means of Monte Carlo simulations of a microscopic model that can take into account both the structural effects and the diffusional aspect simultaneously. Microscopic simulations of structures were first started by Anderson et al.[5] who developed a Monte Carlo statistical mechanics model to study the grain growth behavior of a fully dense system, in which

structures were mapped onto domains of vectors of different orientations. A grain is a domain of vectors with the same orientation. Grain growth in this model took place by flipping the orientations of the vectors simulated with a Monte Carlo algorithm. The Monte Carlo simulations of this vector model allowed the statistical mechanics of microstructures to be taken into account and their simulations were capable of showing various desired scenarios of grain growth such as the movement of the grain boundaries in the direction of the concave curvature, the increase of the grain size in a power-law fashion with time with an exponent between 0.3 and 0.5, and a time-independent normalized grain-size distribution during grain growth.

Compared to grain growth of a fully dense system, sintering is a more complicated phenomenon in that it involves not only the orientational changes but also the diffusion of matter (or vacancies) in a powder/pore network. Grain boundaries may act as vacancy pipes or as vacancy sinks depending on the lattice vacancy concentration, the pore size, and the location of the pore with respect to a grain boundary.[6] A microscopic sintering model must take into account both the micro-structures and the diffusional aspect. Recently, Chen et al.[7] have incorporated domains of vacancies as pores into the model of Anderson et al.[5] to study the final-stage sintering. However, vacancies in this model did not actually move; but, the densification was accomplished by removing vacancies from pores at their junctions with grain boundaries. The pore-shrinkage probability was obtained from a macroscopic derivation with a presumed pore geometry and therefore, pores in this model can only shrink.[7]

In the present paper, in addition to orientational flipping, we incorporate diffusion of vacancies into the simulations. By allowing the vacancies to move, we are able to examine the microstructural effects on sintering more generally. For the orientational changes, we employ the vector-vacancy model where a domain of vectors of the same orientation is a grain and a domain of vacancies is a pore. By incorporating the outer surfaces of the samples in the simulations and allowing vacancies to move, densification of a sample is a result of the diffusion of vacancies away from the pores to the outer sample surfaces. The movement of a vacancy is achieved by exchanging it with one of its neighboring vectors and is simulated with the Monte Carlo method. The movement of a vacancy may also be viewed as a movement of matter in the opposite direction. As vacancies can move away from a pore, they can also move into a pore. Therefore, in addition to pore shrinkage, our model is also capable of exhibiting pore growth and pore coalescence as in a real system.

Simulations have been carried out in two dimensions and showed that the model is indeed capable of

exhibiting various desired features of sintering such as densification, growth of large pores, pore coalescence, evaporation and condensation, rounding of a sharp corner, grain growth, neck formation, and thermal etching of grain boundaries.

To clearly illustrate the effect of different grain size/pore size ratios, we investigated the sintering behavior of an isolated pore. By single-pore simulations, we exclude the effect of interpore interactions and focus on the effect of different grain size/pore size ratios on pore sintering. The effect of interpore interactions on the sintering of a multipore compact will be addressed in subsequent publications. For the sintering of an isolated pore, the most salient result is that the scaling relationship for the pore elimination time t_p with respect to the pore diameter d_p changes when d_p changes from larger than the grain diameter G to smaller than G. This is a result of the grain boundaries serving as diffusion channels in a fine-grain microstructure such as those considered in the simulations. In the sample-size-fixed simulations where the sample size was kept fixed, we show that for $d_p > G$, the pore shrinkage rate is independent of d_p and proportional to $1/G$ whereas for $d_p < G$, the pore shrinkage rate becomes independent of G but proportional to $1/d_p$ where the pore shrinkage rate is the rate of change in the pore area. Consequently, the pore elimination time t_p shows two distinct power laws with respect to d_p: $t_p \sim d_p^3$ for $d_p < G$ and $t_p \sim d_p^2$ for $d_p > G$ in sample-size-fixed simulations. The crossover pore diameter d_c, i.e., the pore size that signifies the change from one scaling relationship to another, increases roughly linearly with G. In sample-size-scaled simulations where the sample size scales in proportion to the initial pore diameter d_p, $t_p \sim d_p^4$ for $d_p < G$ and $t_p \sim d_p^3$ for $d_p > G$, indicating a linear dependence of t_p on the sample size. A scaling analysis is provided to explain the simulated results relating the pore elimination time to the pore size. The scaling analysis is similar to Herring's scaling theory[8] but is derived for systems with grain-boundary diffusion. We further show that these scaling relations are independent of dimensionality. Thus, the results of the two-dimensional simulations should also hold in three dimensions.

The rest of the paper is organized as follows. Sections II and III describe the model and the simulation procedures, respectively. The results of the simulations are contained in Sec. IV. Sec. V gives the detail of the scaling analysis and Sec. VI, the concluding remarks.

II. MODEL

The statistical mechanics model that we employ in the present study is composed of vectors of different orientations and vacancies.[7] In addition to the application for final-stage sintering, it has also been successfully

applied to study grain-boundary wetting.[9] As in Ref. 7, we map a microstructure onto a discrete lattice, as shown in Fig. 1. A lattice site can be a portion of a grain as denoted by a letter or a portion of a pore as denoted by an empty site. Each letter represents a crystalline orientation. A domain of the same letter represents a grain and a domain of vacancies, a pore. There are N possible crystalline orientations. For simplicity, we take the N crystalline orientations to be N planar vectors uniformly spaced on a circle with the angle of a vector a multiple of $2\pi/N$. The interaction between two vectors depends on the angle difference θ of the two vectors, and, in general, can be any reasonable function. In the present study, we take

$$V(\theta) = E_{gb} \quad \text{if } \theta \neq 0$$
$$= 0 \quad \text{if } \theta = 0. \tag{1}$$

We consider only the nearest-neighbor interactions; i.e., only the interactions between adjacent lattice sites can be non-zero. The interaction between a vector and a vacancy (empty site) is E_s and the interaction between two vacancies is zero. With these definitions, the solid-vapor interfacial energy at $T = 0$ K is proportional to E_s and the grain-boundary energy at $T = 0$ K is proportional to E_{gb}. Therefore, the ratio of E_s/E_{gb} determines the $T = 0$ K dihedral angle Ψ by $\Psi = 2 \cos^{-1}(2E_s/E_{gb})$. For example, $E_s/E_{gb} = 5/3$ gives $\Psi = 145°$.

III. MONTE CARLO SIMULATIONS

Monte Carlo simulations[10] can be a powerful tool for the kinetic study of a statistical mechanics model when an appropriate kinetic procedure is chosen. We include (i) the orientational flipping of vectors to simulate microstructural changes such as grain growth and (ii) vacancy diffusion to give rise to sintering
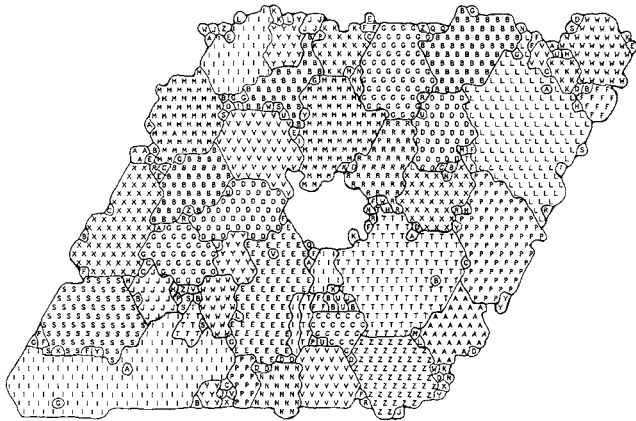

FIG. 1. A lattice representation of a structure. A domain of a same letter is a grain and a domain of empty sites is a pore. Each letter denotes a different crystalline orientation.

A. Orientational flipping

Given a microstructure (with vectors and vacancies), an occupied site, i.e., a vector is randomly chosen. Before the vector is allowed to change its orientation, it first breaks its bonds with its neighboring vectors that have the same orientation as the vector. Breaking each of such bonds costs E_{gb}. Therefore, the total energy cost ΔE to break all such bonds is $\Delta E = nE_{gb}$ where n is the number of neighboring vectors that have the same orientation as the vector, and whether the vector will successfully break its bonds with its neighbors is determined by the transition rate

$$W = (1/\tau_G)e^{-\Delta E/kT} \quad \text{if } \Delta E > 0$$
$$= 1/\tau_G \quad \text{if } \Delta E \leq 0, \tag{2}$$

where $1/\tau_G$ is the attempt frequency associated with orientational flipping, k the Boltzmann constant, and T the sintering temperature. Equation (2) is simulated as follows. In each attempt for bond breaking, the energy cost ΔE is calculated and the Boltzmann factor $e^{-\Delta E/kT}$ will be compared to a random number between 0 and 1. If the Boltzmann factor $e^{-\Delta E/kT}$ is larger than or equal to the random number, the vector breaks its bonds with its neighboring vectors and slips to a new orientation which is picked by another random number. If the Boltzman factor $e^{-\Delta E/kT}$ is smaller than the random number, the orientation of the vector remains unchanged.

B. Vacancy diffusion

Sintering of a porous object requires transporting vacancies out of the object. In order to study sintering from a microscopic perspective, diffusion of vacancies must be incorporated in the simulations. Vacancy diffusion in our simulations is modeled as a sequence of random translational movements of vacancies. When a vacancy is adjacent to at least one vector, it may undergo a random translational movement as follows. First, one of the vacancy's neighboring vectors is chosen at random. The transition rate W_{ex} for exchanging the position of the vacancy with that of the chosen vector is

$$W_{ex} = (1/\tau_D)e^{-\Delta E_{ex}/kT} \quad \text{if } \Delta E_{ex} > 0$$
$$= 1/\tau_D \quad \text{if } \Delta E_{ex} \leq 0, \tag{3}$$

where $1/\tau_D$ is the attempt frequency for vacancy diffusion and ΔE_{ex} is the energy change associated with the exchange, which depends on the parameters E_s and E_{gb} as well as the neighboring configuration of the vector-vacancy pair before and after the exchange. To achieve the transition rate depicted in Eq. (3), the simulation is done as follows. In each trial for a position exchange, the energy change ΔE_{ex} as well as the Boltzmann factor $e^{-\Delta E_{ex}/kT}$ are calculated. If the Boltzmann factor $e^{-\Delta E_{ex}/kT}$ is larger than or equal to a random number between 0 and 1, the position of the vacancy will be

exchanged with that of the chosen neighboring vector. If the Boltzmann factor $e^{-\Delta E_{ex}/kT}$ is smaller than the random number, the position of the vacancy and that of the vector will remain unchanged. An example is shown in Figs. 2(a) and 2(b) to illustrate how ΔE_{ex} is calculated. The movement of a vacancy may also be viewed as a movement of matter in the opposite direction. The attempt frequency $1/\tau_D$ for vacancy diffusion can be different from that for orientational flipping, $1/\tau_G$, depending on the material. The ratio τ_D/τ_G can be used to control the grain growth rate relative to densification in the simulations. A small τ_D/τ_G corresponds to a system with slow grain growth. By allowing vacancies to move and by incorporating the outer surfaces in the simulations, densification of a sample will take place through the diffusion of vacancies away from the pores to the outer surfaces of the sample.

IV. RESULTS

For the present studies, we chose $N = 30$ and $E_s/E_{gb} = 1.67$ (equivalent to a 145° dihedral angle at $T = 0$ K). Simulations were all carried out at $T = 0.8\ T_m$ where $T_m = 0.83\ E_{gb}$ is the melting temperature estimated by mean-field approximations.[9] For a large value of N such as the one we used, the melting temperature estimated by the mean-field approximations should be as good as that estimated by Monte Carlo simulations.[11] For computational ease, the simulations were carried out in two dimensions on a triangular lattice with periodic boundary conditions. All the simulation results shown in this paper were averaged over 100 independent runs. The Monte Carlo cell is such that the sample is located at the center of the cell and is surrounded by three rows of vacancies (open space) around each edge. Due to the periodic boundary conditions, the system may be thought of as an infinite repetition of the Monte Carlo cell in both the x and the y directions with an edge-to-edge sample distance of six rows. Therefore, under suitable conditions, i.e., at higher temperatures, necking may occur between the upper edge and the lower edge of the sample, which are six rows apart due to the periodic

boundary conditions. Likewise, necking may also occur between the left and the right edges.

A. General features of the model

Figures 3(a)–3(d) illustrate the sintering behavior of a multipore compact. We use $\tau_D/\tau_G = 0.1$ to produce Figs. 3(a)–3(d). Figure 3(a) is the initial configuration with 10% porosity. Figure 3(b) is taken at $t = 2000\ \tau_D$. Note that (i) the entire sample is shrinking compared to Fig. 3(a) due to the transportation of vacancies from the interior of the sample to the outer surfaces of the sample, (ii) some pores are coalescing, and (iii) some of the material has evaporated, as indicated by the arrow. Figure 3(c) is at $t = 4000\ \tau_D$. In this snapshot, it can been seen that part of the surface has ruptured, as indicated by arrow α. Also notice than an initially sharp corner has become rounded, as indicated by arrow β. Figure 3(d) is taken at $t = 50,000\ \tau_D$ when the sample is almost fully densified. Note that (i) grains have grown considerably larger, (ii) the material that has evaporated earlier has recondensed (condensation), (iii) necking has already taken place, as indicated by the arrows on the top and at the bottom due to the periodic boundary conditions (initially the upper edge and the lower edge were separated by six rows of vacancies), and (iv) the opening up of a grain boundary at the surface (thermal etching). Note that although the energy parameters we have chosen should, in principle, give a dihedral angle of 145°, the actual dihedral angles displayed in Figs. 3(b)–3(d) are not quite 145° due to the discrete lattice we used in the simulations. It is clear from Figs. 3(a)–3(d) that our sintering model is indeed capable of showing various essential sintering phenomena, e.g., densification, pore coalescence, necking, thermal etching of the outer surface at a grain boundary, evaporation and condensation, rounding of a sharp corner, and grain growth. The incorporation of the vacancy diffusion in our model indeed catches the microscopic essence of sintering.

B. Elimination of an isolated pore

Sintering of a multipore compact involves many factors. Often the interactions between pores inhibit a clear-cut separation of the effect of one factor from another. In order to avoid pore interactions, we study the sintering of an isolated pore first. While studying the sintering of an isolated pore may be difficult experimentally, it is doable with computer simulations. The closest experiments to the sintering of isolated pores are those of Zhao and Harmer[12] in which they studied the sintering of alumina compacts with very low initial porosity so that the initial pore radii were much smaller than the distances between pores. More recently, Slamovich and Lange[13] have done similar experiments

(a)   (b)

Ei = 4 Es + 2 Egb   Ef = 8 Es
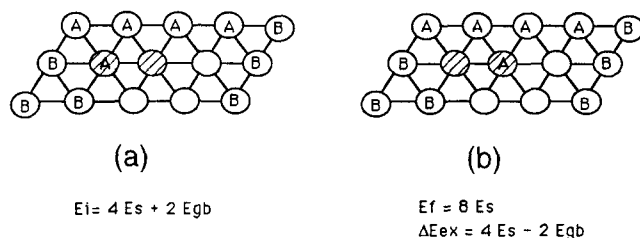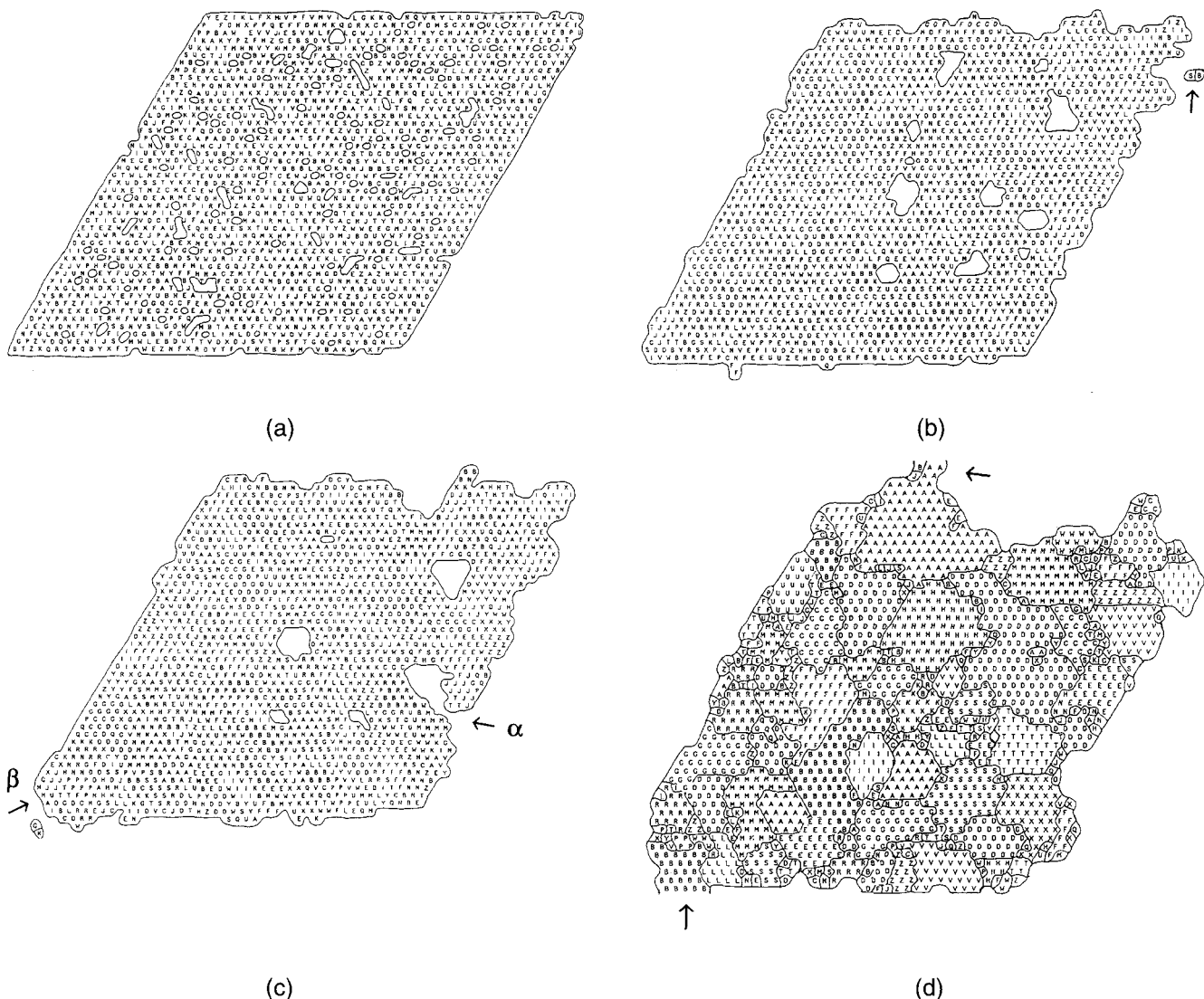 ΔEex = 4 Es - 2 Egb

FIG. 2. An example showing how ΔE_{ex} is calculated. (a) and (b) represent the configurations before and after the position exchange of a vector-vacancy pair, respectively. The vector-vacancy pairs under consideration are shaded. E_i and E_f denote the energy of the vector-vacancy pair before and after the move and $\Delta E_{ex} = E_f - E_i$.

(a)

(b)

(c)

(d)

FIG. 3. A typical structural evolution of a multipore compact; (a) $t = 0$, (b) $t = 2000 \ \tau_D$, (c) $t = 4000 \ \tau_D$, and (d) $t = 50,000 \ \tau_D$.

on yttria doped zirconia systems. The sintering of a pore may depend on several factors such as the pore diameter, the pore shape, and the average grain diameter of the surrounding polycrystalline matrix. In the present geometry, there are no other pores around; the only diffusion distance is that from the pore surface to the outer sample surface. Therefore, pore elimination may also depend on the sample size. The results of the simulations showed that with sufficient sintering time, all pores can be eliminated and the pore elimination time, indeed, depends on all of the above factors. In the following, we will examine each of the above factors.

A typical microstructural evolution during the sintering of an isolated pore is shown in Figs. 4(a)–4(c). Figure 4(a) is the initial configuration with a hexagonal pore at the center where the length of an edge equals 4 with the length expressed in units of the lattice

constant of the underlying lattice. Figure 4(b) is at $t = 2000 \ \tau_D$. As in Figs. 3(a)–3(d), we used $\tau_D/\tau_G = 0.1$ for Figs. 4(a)–4(c). Notice that not only the pore shrank but the shape of the pore also changed. The pore was not longer hexagonal. In sintering experiments, shape changes were also evident.[12-14] Figure 4(c) is at $t = 5000 \ \tau_D$ when the pore is almost completely removed.

The effect of pore diameter and that of pore shape are summarized in Fig. 5 where we plot the pore elimination time t_p as a function of the initial pore area A_p in a double logarithmic scale for various pore shapes. The pore elimination time t_p is the time needed to completely eliminate a pore and is directly obtained from the simulations. To focus on the effect of pore area and pore shape, the result shown in Fig. 5 is obtained at a fixed grain diameter $G = 4.0$ where G is the grain diameter taken as the square root of the average grain area. The
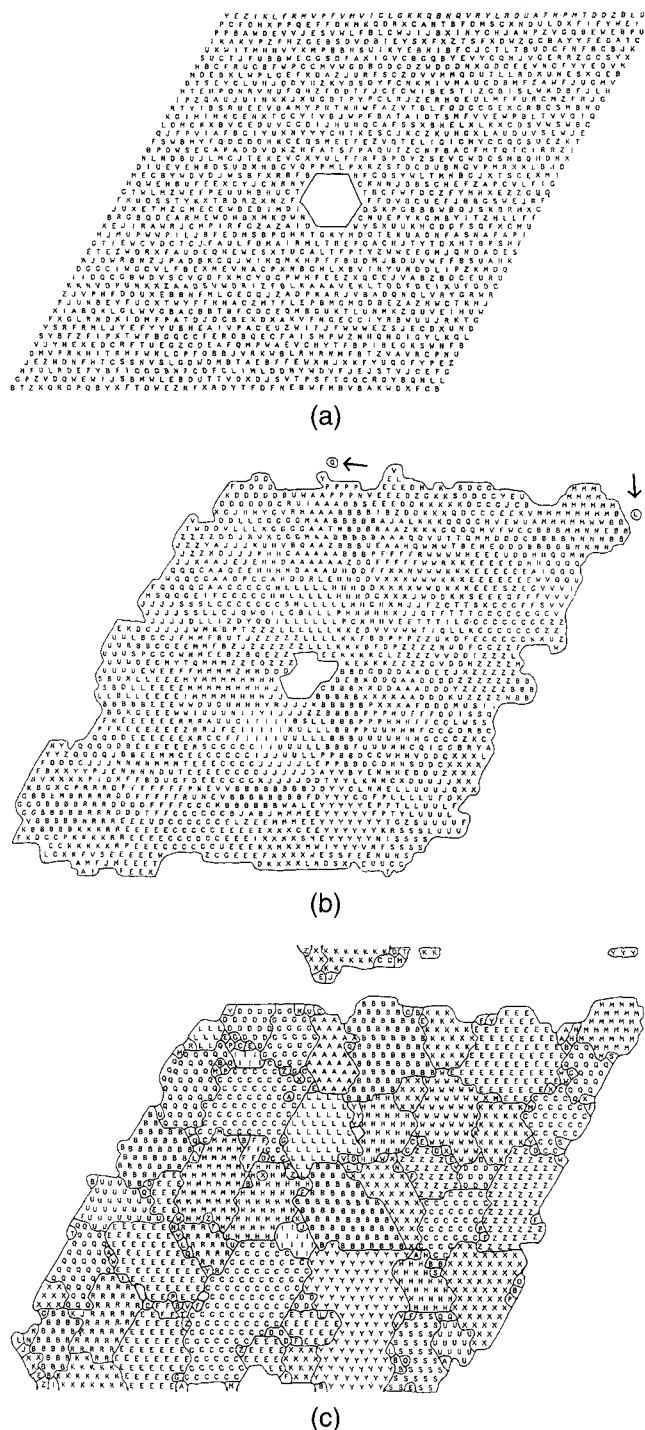
1004

(a)

(b)

(c)

FIG. 4. The structural evolution of an isolated hexagonal pore with edge = 4, at (a) $t = 0$, (b) $t = 2000\ \tau_D$, and (c) $t = 5000\ \tau_D$.
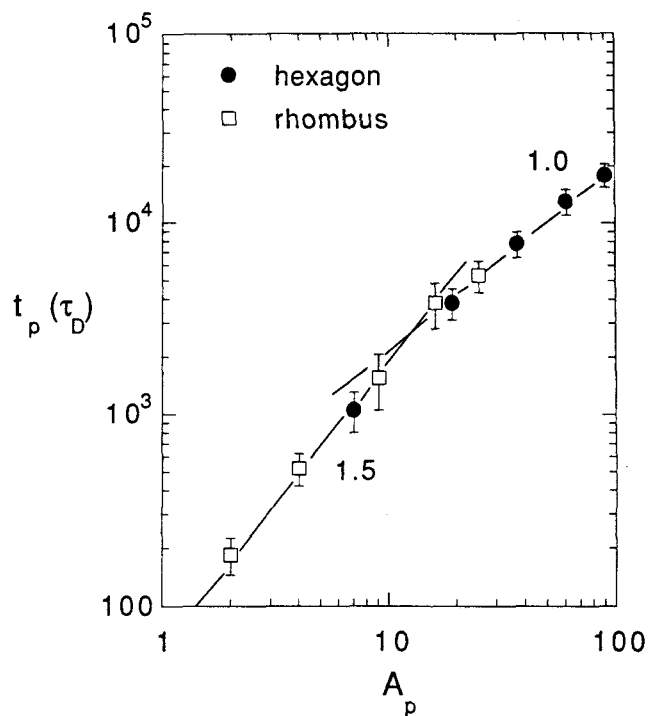

FIG. 5. t_p vs A_p at $G = 4.0$ for fixed sample size 45×45 where t_p and A_p are the pore elimination time and the initial pore area, respectively. Full circles and open squares denote initially hexagonally, and rhombically shaped pores. Notice that all data points fall on the same curve, indicating that the pore elimination time is independent of the initial pore shape.

diameter increases with time as a power law $G \sim t^{0.38}$. A typical G-vs-t plot was shown in Fig. 6. Once the desired grain diameter was reached, sintering of the pore began. To separate the effect of grain growth, we did not allow orientational flipping to occur during sintering. The sample size was fixed at 45×45. Examples of how these pores evolve with time under such conditions are shown in Fig. 7 where the pore area as a function
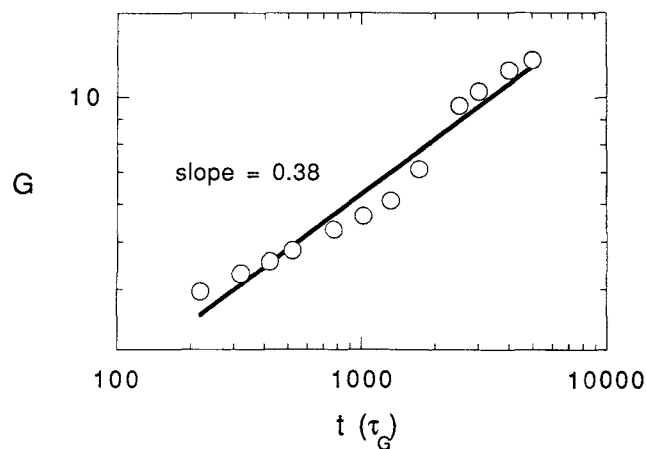

FIG. 6. G vs t where G is the average grain diameter and t is the time in unit of τ_G. The slope of $\ln G$ vs t is about 0.38 for the present model.
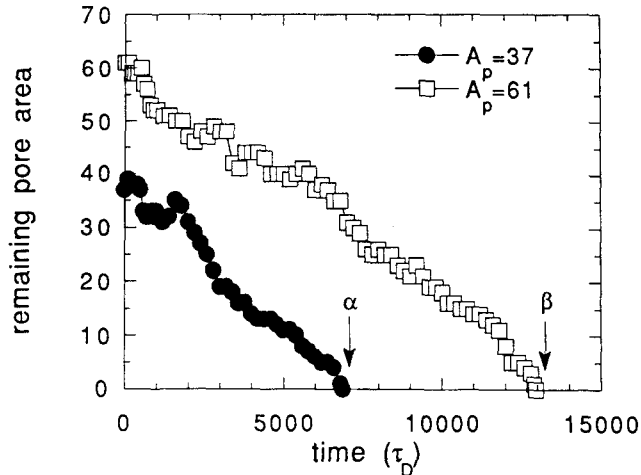
simulation procedure is as follows. We started with a random grain configuration with a pore of a certain area and a certain shape located at the center of the sample as similar to Fig. 4(a). Before the sintering of the pore began, we allowed the orientational flipping to occur for a certain period of time so that grains could grow to the desired diameter. In the present simulations, the grain

FIG. 7. Pore area versus time for two pores. Arrows α and β indicate the pore elimination time t_p for $A_p = 37$ and 61, respectively.

of time is shown for two pores with $A_p = 37$ and 61, respectively. The simulation conditions for Fig. 7 are identical to those for Fig. 5. From Fig. 7, one can see that overall, the pore area decreases with time while some short-lived increases occurred due to the random nature of the diffusional processes. Eventually, both pores were completely eliminated. The pore elimination times t_p for the two pores shown in Fig. 7 are marked by arrow α and arrow β for $A_p = 37$ and 61, respectively.

From Fig. 5, first, note that the pore elimination time t_p is essentially independent of the initial pore shape. This is conceivable since pores undergo shape change during sintering, as we have shown above. Notice that the pore elimination time t_p follows two distinct power laws with respect to the initial pore area A_p: (i) $t_p \sim A_p^{1.0}$ for large pores and (ii) $t_p \sim A_p^{1.5}$ for small pores. A full account for the scaling behavior of the pore elimination time with respect to the initial pore area will be given in the next section with a scaling analysis. Here we will focus on the difference in the scaling laws of the pore elimination time between large pores and small pores. The difference between the scaling law for large pores and that for small pores is a result of grain boundaries serving as diffusion channels in fine-grained microstructures. When the pores are larger than the grains, the number of diffusion channels is proportional to d_p/G where $d_p = A_p^{0.5}$ is the initial diameter of the pore. On the other hand, when the pore is smaller than the grains, the number of diffusion channels becomes independent of d_p/G. This difference in the pore shrinkage rate gives the additional $A_p^{0.5}$ dependence in the pore elimination time for small pores in Fig. 5. More discussions will be given in the next section concerning the different dependence of the number of the diffusional channels on d_p/G at the pore surface between pores larger than the grains and pores smaller

than the grains. Given that the number of the diffusion channels at the pore surface is proportional to d_p/G for pores larger than the grains and is independent of d_p/G for pores smaller than the grains, one would expect that as the grain diameter increases, the crossover pore area A_c below which the small-pore scaling law prevails and above which the large-pore scaling law dominates increases in proportion to G^2. In Fig. 8, we plot the pore elimination time as a function of A_p for a different grain diameter $G = 8.0$. Also plotted is the pore elimination time for $G = 4.0$ for comparison. Again, like the case of $G = 4.0$, the pore elimination time for $G = 8.0$ is independent of the initial pore shapes and depends only on the initial pore area. One can see that the small-pore sintering behavior, i.e., $t_p \sim A_p^{1.5}$ persists up to about $A_p \cong 40$ above which the large-pore sintering behavior, i.e., $t_p \sim A_p^{1.0}$ takes over. Indeed, the crossover pore area A_c increases roughly in proportion to the square of the grain diameter from about $A_c \cong 12$ for $G = 4.0$ to about $A_c \cong 48$ for $G = 8.0$.

The effect of the grain diameter G is summarized in Fig. 9 where we plot the remaining pore area A_R at $t = 2000 \ \tau_D$ as a function of the grain diameter G for hexagonal pores of three different initial pore
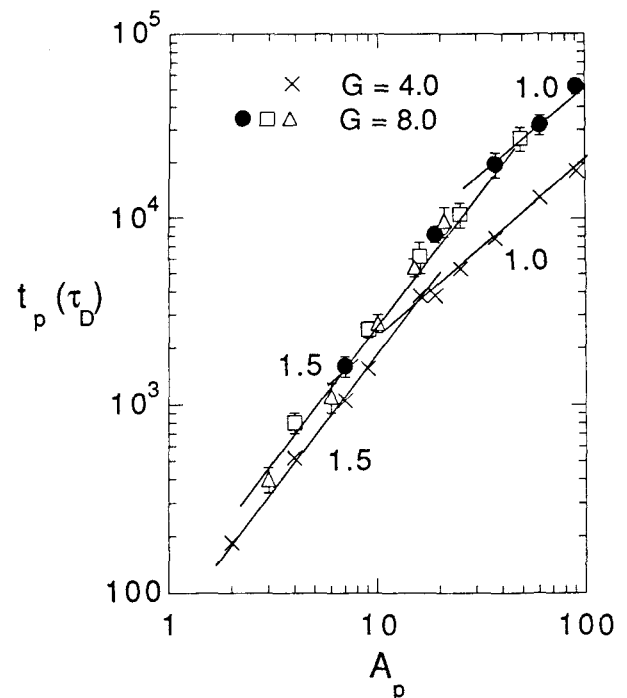

FIG. 8. t_p vs A_p at $G = 8.0$ for fixed sample size 45×45 where t_p and A_p are the same as defined in Fig. 4. Full circles, open squares, and open triangles denote initially hexagonally, rhombically, and triangularly shaped pores. Again, the data points of pores with different initial shapes all fall on the same curve, indicating that the pore elimination time is independent of the initial pore shape. The crosses are the same data points as in Fig. 4 for $G = 4.0$ shown here for comparison.
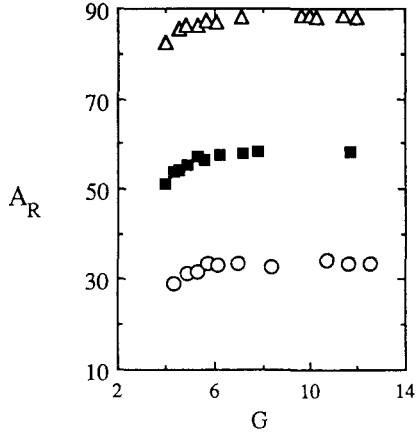
1006

FIG. 9. A_R vs G where A_R is the remaining pore area at $t = 2000\ \tau_D$ and G is the average grain diameter. Open circles, full squares, and open triangles denote $A_p = 37$, 61, and 91, respectively.

area: open circles, full squares, and open triangles for $A_p = 37$ (edge = 4), 61 (edge = 5), and 91 (edge = 6), respectively. Notice that on the average, pores shrank after 2000 τ_D and there exist two regimes for the pore shrinkage rate. (i) At small G, the shrinkage of pores decreases as G increases and (ii) at large G, A_R flattens out. The boundary between two regimes occurs at about $G \cong d_p$. In order to better illustrate this, we plot ΔA as a function of d_p/G in Fig. 10 where $\Delta A = A_p - A_R$ is the average decreased in the pore area at $t = 2000\ \tau_D$. Notice that ΔA increases linearly with d_p/G when $d_p > G$ and ΔA becomes a constant when $d_p < G$. The linear dependence of ΔA on d_p/G at $G < d_p$ evidences that grain boundaries serve as diffusion channels in the present simulations. A constant ΔA for large G indicates that the number of diffusion channels becomes
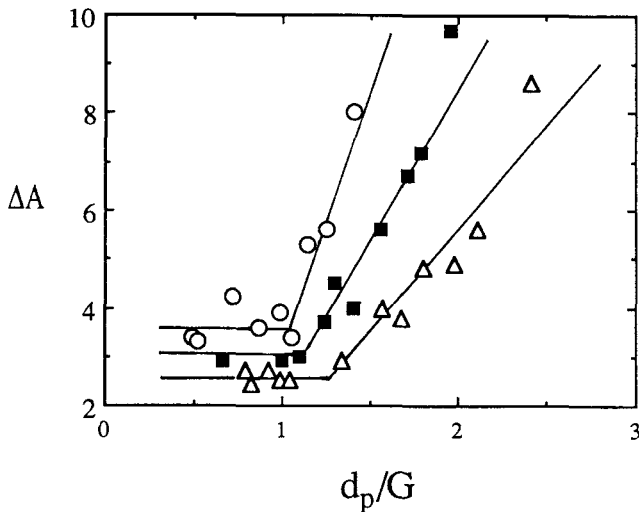
independent of G when grains are larger than the pores. The different slopes of ΔA-vs-(d_p/G) of the three curves in Fig. 10 are due to the different values of A_p. In fact, under the present simulation geometry, the pore shrinkage rate is independent of d_p and only proportional to $1/G$ for $d_p > G$. For $d_p < G$, the shrinkage is independent of G and only proportional to $1/d_p$. In Fig. 11(a), we replot ΔA as a function of $1/G$. Indeed, for large $1/G$ (small G), ΔA vs $1/G$ of $A_p = 37, 61$, and 91 all fall on the same straight line whereas for small $1/G$ (large G), ΔA is independent of G and decreases with increasing d_p. A blow-up for the small $1/G$ region in Fig. 11(a) is shown in Fig. 11(b) with the vertical axis as $\Delta A d_p/d_1$ and the horizontal axis as $1/G$ where d_1 is the initial diameter for $A_p = 37$. Indeed, $\Delta A d_p/d_1$ is a constant, indicating that in the small $1/G$ region, ΔA is independent of G and inversely proportional to d_p. A more detailed explanation will be provided with

FIG. 10. ΔA vs d_p/G for the data shown in Fig. 9. $\Delta A = A_p - A_R$ is the decrease in pore area at $t = 2000\ \tau_D$ and $d_p = A_p^{0.5}$ is the initial pore diameter. Again, open circles, full squares, and open triangles denote $A_p = 37$, 61, and 91, respectively.
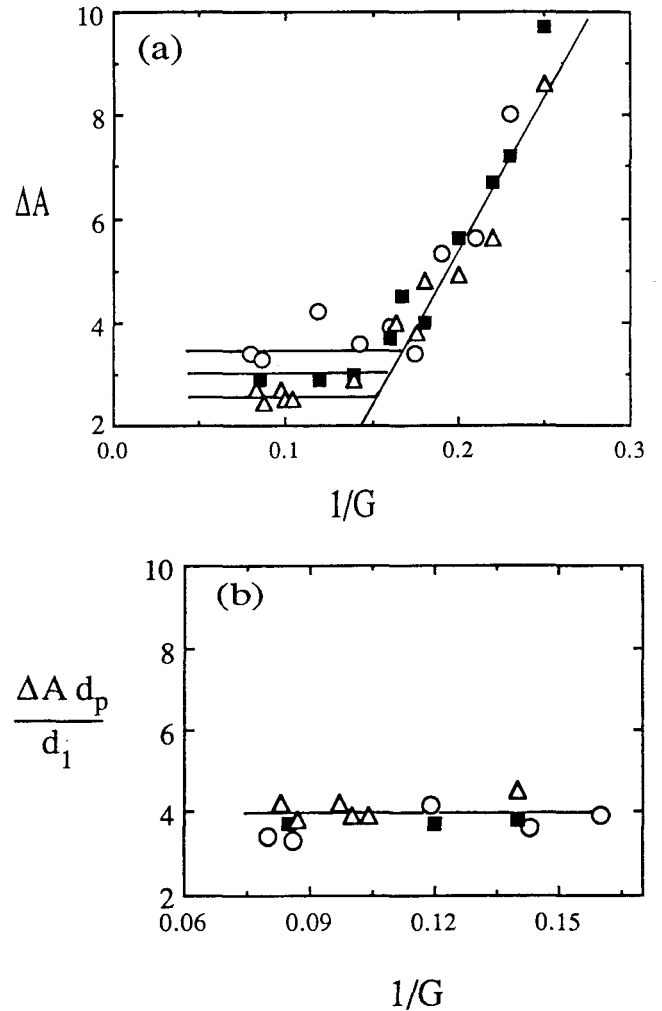

FIG. 11. (a) ΔA vs $1/G$ for the data shown in Fig. 10 and (b) $\Delta A d_p/d_1$ vs $1/G$ for the small $1/G$ region in (a). ΔA and d_p are the same as defined in Fig. 10. d_1 is the initial diameter for $A_p = 37$ and G, the average grain diameter. Again, open circles, full squares, and open triangles denote $A_p = 37$, 61, and 91, respectively.

a scaling theory in the following section. The different scaling laws for the pore elimination time as a function of the initial pore area between pores larger than the grain and pores smaller than the grain shown in Figs. 5 and 8 are reminiscent of the different pore shrinkage rates with respect to grain diameter between pores larger than the grains and pores smaller than the grains, as shown in Figs. 9–11 and are the result of grain boundaries serving as diffusion channels in the present simulations.

Qualitatively, the reason that the grain boundaries serve as diffusion channels in the present model is the following. In order for the pores to shrink, (1) vacancies must first break up with a pore and (2) vacancies must diffuse away. In both processes, vacancies must overcome an energy barrier ΔE_{ex} to exchange their positions with a neighboring vector where the energy barrier ΔE_{ex} is the energy change associated with the exchange, as depicted in Eq. (3). If the vector involved is on a grain boundary, ΔE_{ex} is reduced due to the fact that a vector on a grain boundary has a higher initial energy as depicted by Eq. (1) and hence a smaller ΔE_{ex}. This is illustrated in Figs. 12 and 13. Figures 12(a) and 12(b) illustrate an example when a vacancy breaks up with a pore and moves into a grain, i.e., by exchanging its position with that of a vector that is not

on a grain boundary (not surrounded by vectors with different orientations). Figures 12(c) and 12(d) illustrate an example when the vacancy breaks up with the pore at a grain boundary, i.e., by exchanging its position with that of a vector that is on a grain boundary (surrounded by at least one vector that has a different orientation). Comparing the ΔE_{ex} of the two processes, one can see that the process in which the vacancy moves into a grain boundary has a lower ΔE_{ex}. Figures 13(a) and 13(b) illustrate an example when a vacancy that is initially on a grain boundary moves into a grain, and Figs. 13(c) and 13(d) show an example when a vacancy moves along a grain boundary. It is clear that ΔE_{ex} is lower when a vacancy moves along a grain boundary. Therefore, vacancies tend to break up with a pore at the junction of a grain boundary with the pore surface and also tend to move along a grain boundary in the subsequent movements. Thus, in fine-grained structures such as the ones considered in the simulations, grain boundaries effectively serve as the channels for the transportation of vacancies away from the pores.

The effect of sample size was analyzed by comparing the scaling law of the pore elimination time t_p with A_p of the sample-size-fixed simulations to those obtained with the sample size varying in proportion to

(a)

Ei= 4 Es

(b)

Ef = 8 Es + Egb

ΔEex = 4 Es + Egb

(c)

Ei= 4 Es + 2 Egb

(d)

Ef = 8 Es + Egb
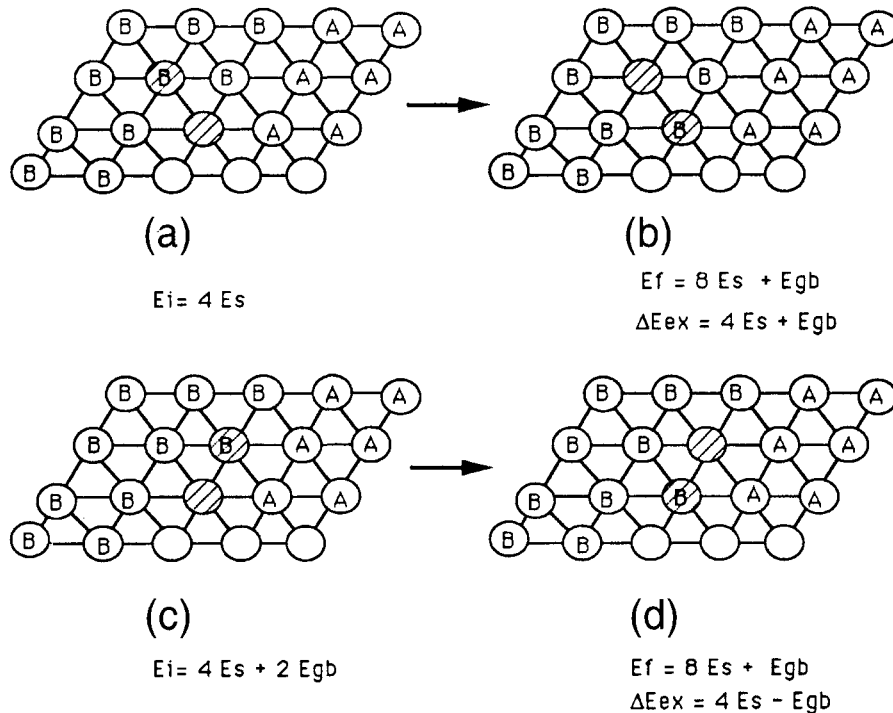
ΔEex = 4 Es - Egb

FIG. 12. (a) and (b) show an example when a vacancy breaks up with the pore by moving into a grain where (a) and (b) represent the configuration before and after the move, respectively. Meanwhile, (c) and (d) represent an example when a vacancy breaks up with the pore at a grain boundary where (c) and (d) represent the configuration before and after the move, respectively. The vacancy-vector pairs that are under consideration for the move are shaded in all figures. E_i and E_f denote the energy of the vector-vacancy pair before and after the move and $\Delta E_{ex} = E_f - E_i$. One can see that ΔE_{ex} is lower when a vacancy breaks up with the pore at the junction of a grain boundary [(c) to (d)] than at a grain surface [(a) to (b)].

d_p. The pore elimination time t_p as a function of A_p for sample-size-scaled simulations is shown in Figs. 14(a) and 14(b). Figure 14(a) shows that $t_p \sim A_p^{2.0}$ for small pores and Fig. 14(b) shows $t_p \sim A_p^{1.5}$ for large pores. Also plotted in Figs. 14(a) and 14(b) for comparison are t_p-vs-A_p results for sample-size-fixed simulations. From the comparison of the results of the sample-size-fixed simulations to that of sample-size-scaled simulations, it is clear that changing the sample size in proportion to the pore diameter gives the additional $A_p^{0.5}$ dependence, meaning that the pore elimination time is linearly proportional to the sample size in the present geometry.

It is worth noting that the simulation results indicate that pore sintering is a kinetics-dominated phenomenon rather than one solely governed by thermodynamics[4] since the simulations showed that all pores were eliminated given a sufficient amount of time and that for a given grain size, it takes longer to eliminate larger pores despite their higher pore-grain coordination number. This is in line with the experimental observations of Zhao and Harmer[12] and Slamovich and Lange.[13] However, note that although on the average, pore area decreases with time as shown in Figs. 5, 8–14, some of the larger pores can actually grow at some intermediate time. Examples are shown in Figs. 15(a)–15(d), all of which were taken at $t = 2000\ \tau_D$. Figures 15(a) and

15(b) evolved from an initial pore area $A_p = 61$ at $G = 5.7$. The remaining pore area $A_R = 48$ in Fig. 15(a) is smaller than the initial pore area whereas the remaining pore area $A_R = 62$ in Fig. 15(b) is larger than the initial pore area. Figures 15(c) and 15(d) evolved from an initial pore area $A_p = 127$ at $G = 16$. The remaining pore area $A_R = 113$ in Fig. 15(c) is smaller than the initial pore area whereas the remaining pore area $A_R = 128$ in Fig. 15(d) is larger than the initial pore area. Note that this pore growth phenomenon is more evident with larger pores. With smaller pores, we see less pore growth. As A_p becomes larger than 60, we begin to observe pore growth and the occurrence of pore growth becomes more frequent as A_p becomes larger. The observed growth of some of the large pores can be explained as follows. The diffusional process involved in sintering is a thermally activated random process. The randomness of the diffusional process allows the possibility of a pore to expand at some finite time. This is especially so for large pores where the macroscopic driving force for shrinkage which is related to the curvature of the pore surface is reduced. It should be noted that the observed pore growth for larger pores is only a temporary phenomenon due to the random nature of the diffusional process. As we have shown above, given a sufficient amount of time, all pores will eventually be eliminated, as the macroscopic driving

(a)

Ei = 6 Es + Egb

(b)

Ef = 6 Es + 4 Egb

ΔEex = 3 Egb

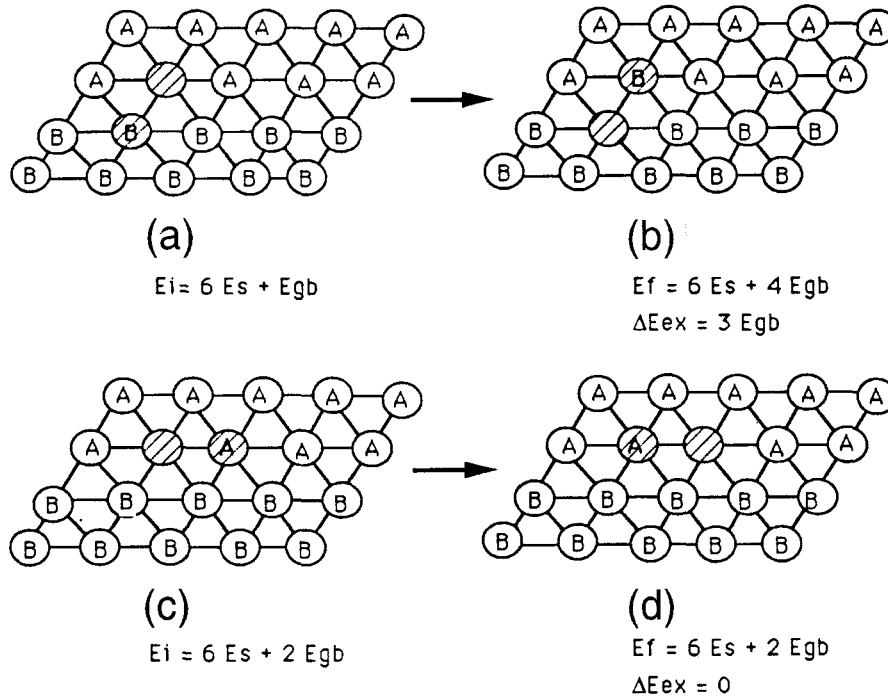(c)

Ei = 6 Es + 2 Egb

(d)

Ef = 6 Es + 2 Egb

ΔEex = 0

FIG. 13. (a) and (b) show an example when a vacancy that is initially on a grain boundary moves into a grain where (a) and (b) represent the configuration before and after the move, respectively. Meanwhile, (c) and (d) represent an example when a vacancy that is initially on a grain boundary moves along the grain boundary where (c) and (d) represent the configuration before and after the move, respectively. The vacancy-vector pairs that are under consideration for the move are shaded in all figures. E_i and E_f denote the energy of the vector-vacancy pair before and after the move and $\Delta E_{ex} = E_f - E_i$. One can see that ΔE_{ex} is lower when a vacancy moves along a grain boundary [(c) to (d)] than into a grain [(a) to (b)].

force consideration would suggest. This can also be seen clearly in Fig. 7. Owing to the statistical mechanical nature of the diffusional process, care must be taken when comparing simulations (or experiments) with a macroscopic theory. It is essential to do proper averaging with sufficient sampling when comparing the results of simulations or experiments to a macroscopic theory that intrinsically deals with statistically averaged quantities. This is why the results shown in this paper were all averaged over at least 100 independent runs. The scaling behaviors of the pore elimination time and that of the pore shrinkage rate we have shown above would not be clear if we had not had enough independent runs for averaging.

Finally, what drives the vacancies to leave the pore than entering the pore is the curvature (Kelvin) effect. To illustrate the curvature effect in the model, let us compare the energy of a vector right beneath a pore surface to that of a vector right beneath a flat surface. For simplicity, let us consider the solid to be single crystalline. A flat interface is depicted in Fig. 16(a) while Figs. 16(b), 16(c), and 16(d) show the pore surface of a hexagonal pore with $A_p = 1$, 7, and 19, respectively. (The corresponding edge length $L = 1$, 2, and 3, respectively.) Let E_{vet} denote the energy of a vector right beneath a vacancy-vector interface. For pore

surfaces such as those shown in Figs. 16(b)–16(d), E_{vet} is calculated by dividing the sum of the energies of all the vectors that are on the pore surface by the number the vectors on the pore surface. Thus, $E_{vet} = 2.0$, 1.0, 1.5, and 1.67 E_s for Figs. 16(a), 16(b), 16(c), and 16(d), respectively. It can be seen that E_{vet} is lower at a pore surface and that E_{vet} decreases with a decreased pore size, i.e., L. Thus, for a vector, being located right beneath a flat interface on the edges of the sample is less energetically favorable than being located right beneath a pore surface, providing the driving force for vectors on the edges of the sample to diffuse to the pore surface (or for vacancies on the pore surface to diffuse to the sample edge), resulting in pore shrinkage. Moreover, with $E_{vet,0}$ defined as the energy of a vector right beneath a flat surface, the correlation between $\Delta E_{vet} \equiv E_{vet} - E_{vet,0}$ of a hexagonal pore and the length of the pore edge L is also summarized in Table I. It is clear that ΔE_{vet} is inversely proportional to L. Note that the radius r_p of a hexagon is proportional to the length of its edge. Moreover, E_{vet} is essentially the Gibbs free energy per vector at $T = 0$ K. Therefore, that ΔE_{vet} is inversely proportional to L is reminiscent of the Kelvin effect; i.e., the Gibbs free energy difference of an atom beneath a surface with a radius of curvature R with respect to that of an atom beneath a flat surface is inverse proportional
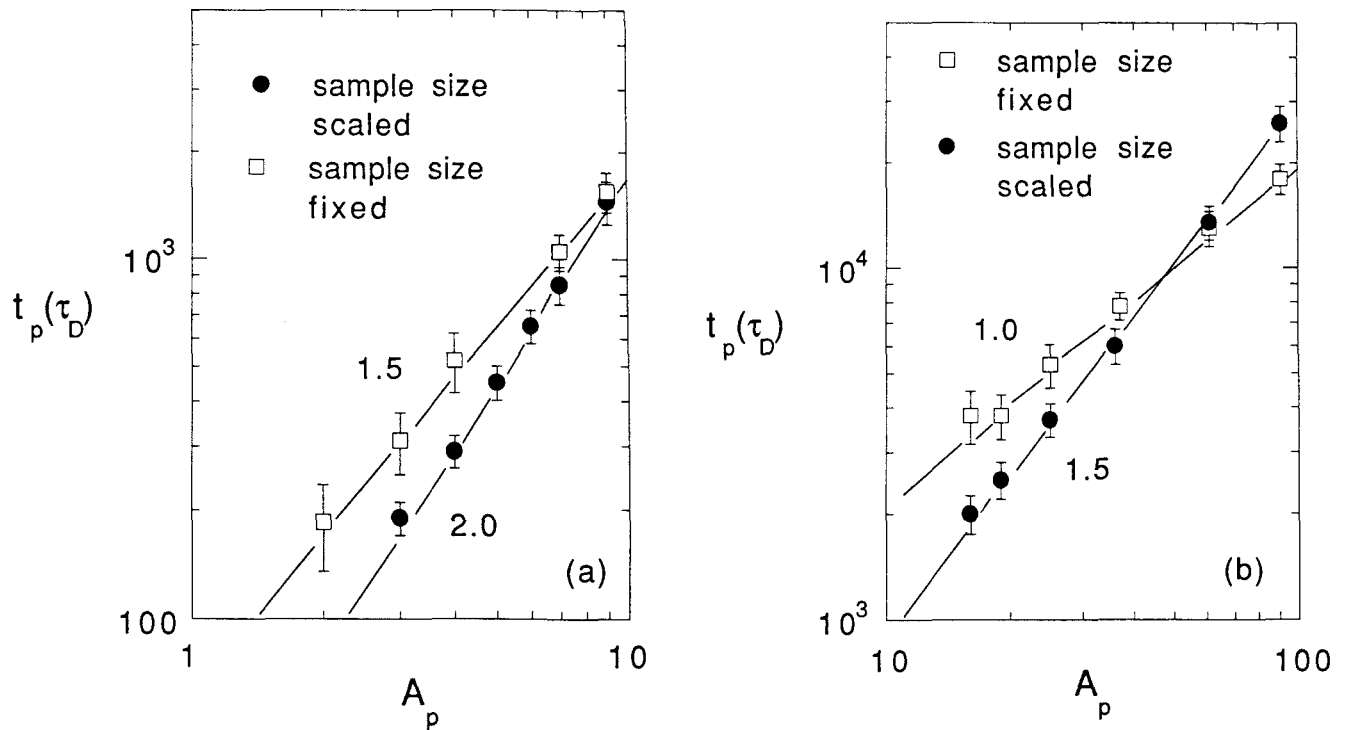

FIG. 14. t_p vs A_p at $G = 4.0$ (a) for small pores and (b) for large pores. t_p and A_p are the same as defined in Fig. 4. Full circles represent data points obtained with sample size scaled in proportion to the initial pore diameter. Also shown are the data points obtained with a fixed sample size 45 × 45 (open squares) for comparison.

TABLE I. E_{vet} represents the energy of a vector right beneath the surface of a hexagonal pore within a single crystal as depicted in Figs. 16(b)–16(d) for $A_p = 1, 7,$ and 19. A_p is the pore area and L is the length of an edge of the pore $\Delta E_{vet} \equiv E_{vet} - E_{vet,0}$ with $E_{vet,0}$ as the energy of a vector right beneath a flat surface, as depicted in Fig. 16(a).

A_p	L	E_{vet} (E_s)	ΔE_{vet} (E_s)	$\Delta E_{vet} L$	
1	1	1	−1.0	−1	Fig. 16(b)
7	2	1.5	−0.5	−1	Fig 16(c)
19	3	1.67	−0.33	−1	Fig. 16(d)
37	4	1.75	−0.25	−1	Not shown

to R. The Kelvin (or curvature) effect arises from the pore geometry but not from any artificial constrains. The curvature effect is the essence both in Herring's scaling analysis and in ours that is described in the next section.

V. SCALING ANALYSIS

In order to understand the scaling relations observed in the simulations, we provide in the following a scaling analysis similar to Herring's for systems where diffusion takes place mainly through grain boundaries. Consider a two-dimensional polycrystalline sample with a pore sitting at the center of the sample as in the simulations. The pore elimination time t_p can be written as

$$t_p \sim A_p/J \sim d_p^2/J, \qquad (4)$$

where A_p is the initial pore area, $d_p = A_p^{0.5}$ the initial pore diameter, and J the atomic current flow into the pore, and J can be decomposed as
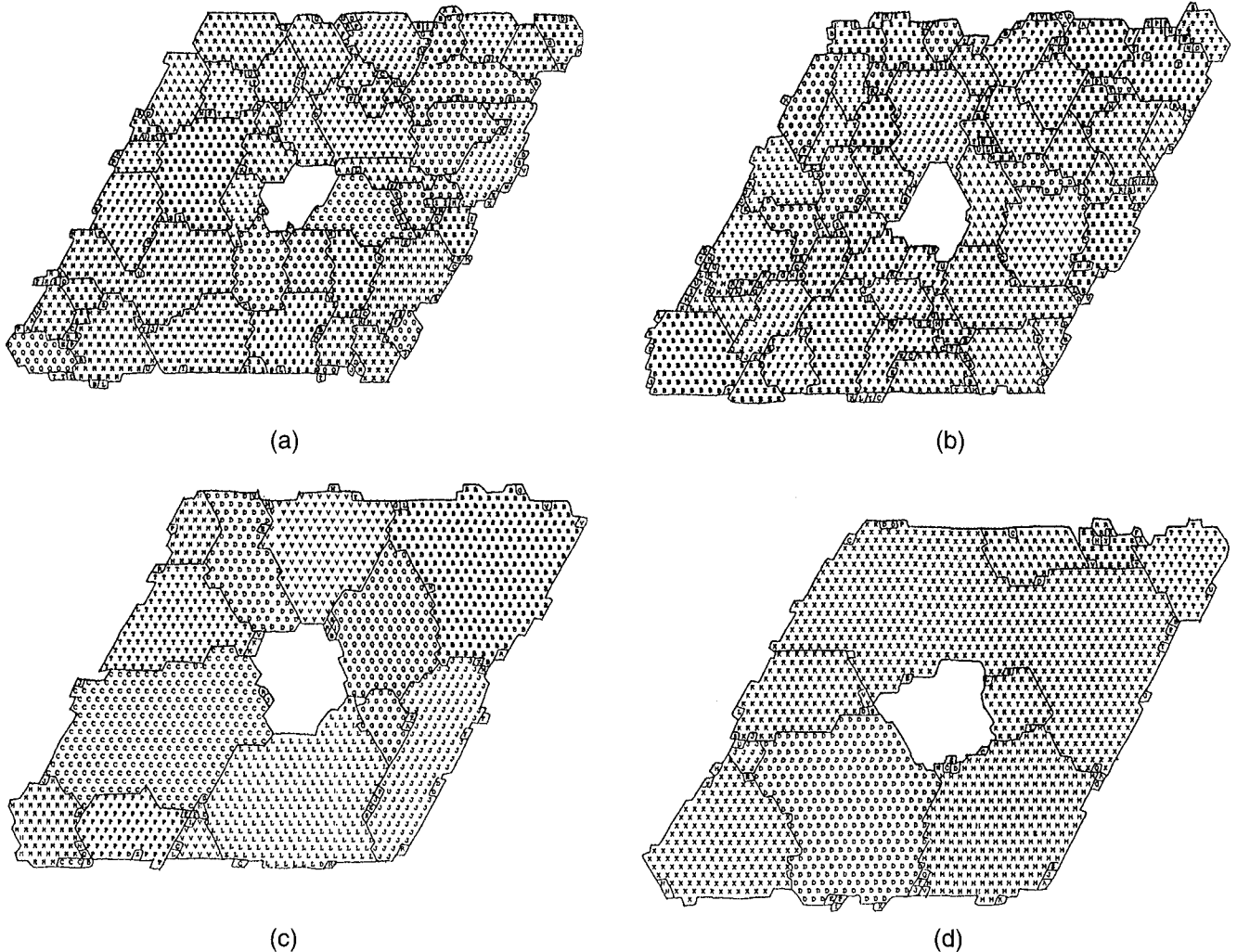
$$J = j \times S, \qquad (5)$$

(a)

(b)

(c)

(d)

FIG. 15. Structures at $t = 2000\ \tau_D$. (a) and (b) evolved from an initial pore area $A_p = 61$ at $G = 5.7$. The remaining pore area $A_R = 48$ in (a) is smaller than the initial pore area whereas $A_R = 62$ in (b) is larger than the initial pore area. (c) and (d) evolved from an initial pore area $A_p = 127$ at $G = 16$. $A_R = 113$ in (c) is smaller than the initial pore area and $A_R = 128$ in (d) is larger than the initial pore area. Note that the pore growth phenomenon occurs more prominently with larger pores.

in which j is the current density at the pore surface defined as the current per unit length and S is the total cross-section length of the grain boundaries at the pore surface. For a sample with a given average grain size G, the total cross-section length S of the grain boundaries with the pore surface should be the product of the cross-section length A_{gb} of an individual grain boundary times the number of grain boundaries intersecting the pore surface. Let us assume that the number of grain boundaries intersecting the pore surface is linear in d_p/G for $d_p > G$ and independent of d_p/G for $d_p < G$. In two dimension, A_{gb} is a constant. Therefore,

$$S \sim A_{gb}(d_p/G)^1 \sim (d_p/G)^1 \quad \text{for } d_p > G, \quad (6)$$

and

$$S \sim A_{gb}(d_p/G)^0 \sim (d_p/G)^0 \quad \text{for } d_p < G. \quad (7)$$

Note that the geometry of the present simulations for $d_p < G$ is comparable to that in Coble's pore sintering theory,[3] namely, the pores are smaller than the grains and are located at junctions of grains. In Coble's theory, the number of grain boundaries intersecting the pore surface is fixed. This is equivalent to saying that the number of grain boundaries is independent of d_p/G. Thus, the

assumption that the number of the grain boundaries intersecting the pore surface is independent of d_p/G for $d_p < G$ is consistent with what was assumed in Coble's theory, which was basically based on experimental observations.[3] While the previous sintering theories did not consider situations for pores larger than the grains, the different scaling laws observed in the present simulations between $d_p < G$ and $d_p > G$ revealed that the dependence of the number of the grain boundaries intersecting the pore surface on d_p/G can be different in the two regimes. As we will show below, by taking into account such difference in the dependence of the number of the grain boundaries intersecting the pore surface on d_p/G between $d_p < G$ and $d_p > G$ and with a proper scaling analysis, one can reproduce the scaling relationships observed in the simulations.

The current density j is related to the diffusivity and the chemical potential gradient of atoms as

$$j = -M\nabla\mu, \quad (8)$$

where $M = Dc/kT$ with D as the diffusion coefficient, c the concentration, k the Boltzmann constant, and T the sintering temperature. In the present simulation geometry, the density j at the pore surface can be
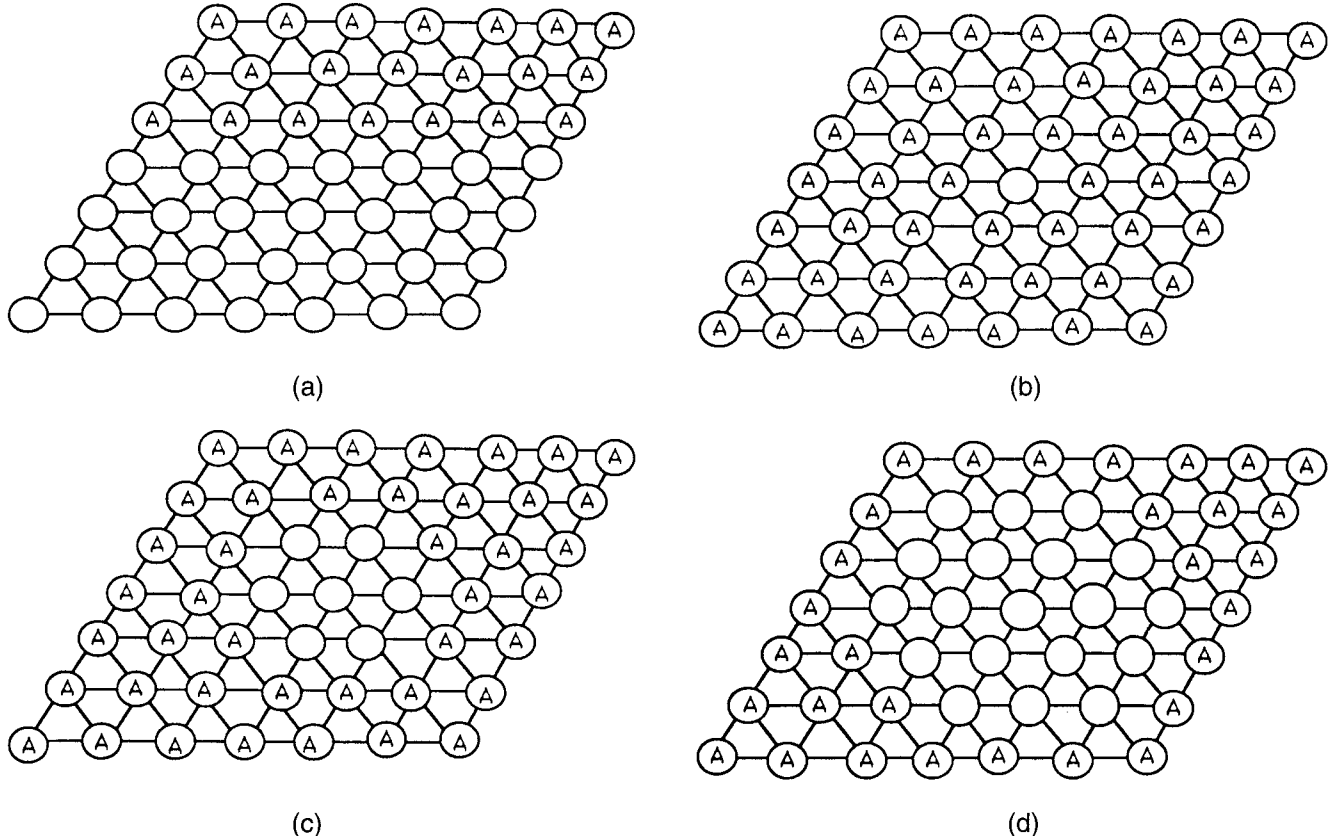

(a)

(b)

(c)

(d)

FIG. 16. The interface between a single crystalline solid as represented by vectors A and the vacuum. (a) represents a flat interface; and (b), (c), and (d) depict the pore surface of a hexagonal pore of $A_p = 1$, 7, and 19, respectively.

approximated as

$$j \sim M(\mu_p - \mu_{\text{out}})/r, \qquad (9)$$

where r is the distance from the pore surface to the outer surface of the sample and μ_p and μ_{out} are the chemical potentials of atoms at the pore surface and that at the outer surface of the sample, respectively. Using the Kelvin equation, the chemical potential of an atom at a curved surface is related to the radius of curvature r_s of the curved surface and the surface tension σ as

$$\mu = \mu_0 + V\sigma/r_s, \qquad (10)$$

in two dimensions where μ_0 is the chemical potential of an atom in the bulk solid phase with a flat surface and V is the atomic area. Therefore,

$$\mu_p - \mu_{\text{out}} \sim 2V\sigma(d_p^{-1} - d_{\text{out}}^{-1}), \qquad (11)$$

where d_p and d_{out} are the diameter of curvature of the pore surface and that of the outer surface of the sample, respectively. The current density j at the pore surface can be rewritten as

$$j \sim (d_p^{-1} - d_{\text{out}}^{-1})/r. \qquad (12)$$

Combining Eqs. (6), (7), and (12), we obtain

$$J \sim (d_p/G)(d_p^{-1} - d_{\text{out}}^{-1})/r \quad \text{for } d_p > G, \qquad (13)$$

and

$$J \sim (d_p^{-1} - d_{\text{out}}^{-1})/r \quad \text{for } d_p < G. \qquad (14)$$

The pore elimination time t_p is then

$$t_p \sim d_p^2 r(d_p/G)^{-1}(d_p^{-1} - d_{\text{out}}^{-1})^{-1} \quad \text{for } d_p > G, \qquad (15)$$

and

$$t_p \sim d_p^2 r(d_p^{-1} - d_{\text{out}}^{-1})^{-1} \quad \text{for } d_p < G. \qquad (16)$$

(i) Size-fixed samples

For size-fixed samples, if the sample size is sufficiently larger than the pore diameter as in the simulations, the outer surfaces can be approximated as flat surfaces, namely, $1/d_{\text{out}} \cong 0$ and the distance r from the pore surface to the outer surface can be regarded as a constant. Therefore, the current density j at the pore surface reduces to

$$j \sim d_p^{-1}. \qquad (17)$$

The total current through the pore surface reduces to

$$J \sim G^{-1} \quad \text{for } d_p > G, \qquad (18)$$

and

$$J \sim d_p^{-1} \quad \text{for } d_p < G. \qquad (19)$$

Note that Eqs. (18) and (19) are indeed in agreement with the shrinkage rate result shown in Figs. 11(a) and 11(b). The pore elimination time for sample-size-fixed simulations reduces to

$$t_p \sim d_p^2(d_p/G)^{-1}d_p \sim Gd_p^2 \quad \text{for } d_p > G, \qquad (20)$$

and

$$t_p \sim d_p^2(d_p^0/G^0)^{-1}d_p \sim d_p^3 \quad \text{for } d_p < G. \qquad (21)$$

One can see that Eqs. (20) and (21) indeed describe the scaling relations observed in the simulations shown in Figs. 5 and 8. The crossover pore diameter d_c can be obtained by equating the right-hand side of Eq. (20) to that of Eq. (21),

$$d_c \sim G. \qquad (22)$$

Again, Eq. (22) is in agreement with the result shown in Fig. 8 where the crossover pore area A_c increases in proportion to G^2.

The agreement between the results of the scaling analysis shown in Eqs. (18)–(22) and the simulation results indicates that the number of diffusion channels is indeed linear in d_p/G for $d_p > G$ and independent of d_p/G for $d_p < G$, as depicted in Eqs. (6) and (7).

(ii) Size-scaled samples

In size-scaled samples, r, d_p, d_{out} all change in proportion. Therefore, the current density j at the pore surface for size-scaled samples becomes

$$j \sim d_p^{-2}. \qquad (23)$$

The total flux for size-scaled samples becomes

$$J \sim (Gd_p)^{-1} \quad \text{for } d_p > G, \qquad (24)$$

and

$$J \sim d_p^{-2} \quad \text{for } d_p < G. \qquad (25)$$

The pore elimination time t_p for sample-size-scaled simulations becomes

$$t_p \sim d_p^2(d_p/G)^{-1}d_p^2 \sim Gd_p^3 \quad \text{for } d_p > G, \qquad (26)$$

and

$$t_p \sim d_p^2(d_p^0/G^0)^{-1}d_p^2 \sim d_p^4 \quad \text{for } d_p < G, \qquad (27)$$

in agreement with the result shown in Figs. 12(a) and 12(b). Note that the scaling relations among the pore elimination time t_p, the pore diameter d_p, and the grain diameter G shown in Eqs. (20)–(21) and (26)–(27) are independent of the dimensionality of the system. This can be shown as follows.

Consider a d-dimensional system. The pore area A_p in Eq. (4) is now replaced by the pore "volume"

$$V_p \sim d_p^d, \qquad (28)$$

where d is the dimension of the system. In two dimensions, the intersections of grain boundaries with the pore surface are an array of dots and the length A_{gb} of each dot is a constant, as depicted in Eqs. (6) and (7). In d dimensions, the intersections of grain boundaries with the pore surface can be approximated as arrays of "lines" and the "area" A_{gb} of each "line" is no longer a constant but dependent on the pore diameter d_p. A_{gb} can be written as

$$A_{gb} \sim w_{gb} d_p^{d-2}, \tag{29}$$

where w_{gb} is the grain-boundary width. Equation (29) satisfies that in two dimensions, these "lines" are actually dots with a constant length A_{gb}, and in three dimensions these "lines" are lines with a width w_{gb} and a length on the order of d_p. For $d_p > G$, there will be an array of d_p/G such "lines" in each of the $d - 1$ dimensions of the pore surface. For $d_p < G$, the number of such "lines" will be constant. Thus, the total cross-section area at the pore surface becomes

$$S \sim (d - 1)(d_p/G)^1 w_{gb} d_p^{d-2} \sim d_p^{d-1} G^{-1}$$
$$\text{for } d_p > G, \tag{30}$$

and

$$S \sim (d_p/G)^0 w_{gb} d_p^{d-2} \sim d_p^{d-2} \quad \text{for } d_p < G. \tag{31}$$

Note that the $(d - 1)$ and G^{-1} dependence in Equation (30) is similar to the relationship[15]

$$S_v = 2/G, \tag{32}$$

between the grain boundary area per unit volume S_v and the average grain diameter G in three dimensions where $d - 1 = 2$ and d_p in Eq. (30) is replaced by unity. Thus, in d dimensions, the total flux becomes

$$J \sim d_p^{d-1} G^{-1}(d_p^{-1} - d_{out}^{-1})/r \quad \text{for } d_p > G, \tag{33}$$

and

$$J \sim d_p^{d-2}(d_p^{-1} - d_{out}^{-1})/r \quad \text{for } d_p < G. \tag{34}$$

The pore elimination time is

$$t_p \sim V_p/J \sim r d_p G(d_p^{-1} - d_{out}^{-1})^{-1} \quad \text{for } d_p > G, \tag{35}$$

and

$$t_p \sim V_p/J \sim r d_p^2(d_p^{-1} - d_{out}^{-1})^{-1} \quad \text{for } d_p < G. \tag{36}$$

One can see that the d_p^d factor in V_p cancels the d_p^d factor in S. As a result, the scaling relations among t_p, d_p, and G do not depend on the dimensionality of the system. Therefore, Eqs. (20)–(21), and (26)–(27) also hold for three dimensions.

It is interesting to note from Eqs. (30) and (31) that the total cross section S of the diffusion channels at the pore surface has a volume-diffusion-like feature, d_p^{d-2} dependence for small pores. These features give rise to the similarity of the scaling relation $t_p \propto d_p^3$ for large pores in our sample-size-scaled simulations to Herring's scaling for volume diffusion, and the similarity of the scaling $t_p \propto d_p^4$ for small pores in our sample-size-scaled simulations to Herring's scaling for surface diffusion. The similarity between the scaling relations observed in our simulations and those of Herring's scaling theory arises from the curvature effect in the chemical potential as we have discussed above, which is essential both in Herring's theory and in our simulations. However, it must be noted that Herring considered lattice diffusion in his theory and there was no consideration of the grain-size effect, whereas in the present simulations, sintering is governed by grain-boundary diffusion.

VI. CONCLUDING REMARKS

We have investigated the grain-size effect on sintering, in particular, the elimination of an isolated pore both with the Monte Carlo simulations and with a scaling analysis. The Monte Carlo simulations were carried out with a general microscopic statistical mechanics model in which microstructures were mapped onto domains of vectors as grains and domains of vacancies as pores. More importantly, we allow vacancies to move in the simulations. By incorporating the outer surfaces of the sample in the simulations, sintering took place via the diffusion of vacancies from the pores to the outer surfaces. The simulations were carried out in two dimensions. The model was shown capable of displaying various sintering phenomena such as evaporation and condensation, rounding of a sharp corner, pore coalescence, thermal etching, neck-formation, grain growth, and growth of large pores. Because of the fine-grained microstructures considered in the simulations, the transport of vacancies was mainly through grain boundaries. We showed that the pore elimination time is independent of the initial pore shape as consistent with the pore-shape change observed during the course of simulation. Experimental observations also support pore-shape change during sintering.[12–14] For $d_p > G$, the pore shrinkage rate is linear in $1/G$ and independent of d_p and for $d_p < G$, the pore shrinkage rate is independent of G and inversely proportional to $1/d_p$, resulting from grain boundaries serving as diffusion channels. The number of grain boundaries intersecting the pore surface is independent of d_p/G for $d_p < G$ and is proportional to d_p/G for $d_p > G$. Another manifestation of the grain-boundary-diffusion mechanism is that the scaling law of t_p with respect to d_p for $d_p > G$ is different from that for $d_p < G$.

For samples with a fixed sample size much larger than the pore size, $t_p \propto d_p^2$ for $d_p > G$ and $t_p \propto d_p^3$ for $d_p < G$. In sample-size-scaled simulations $t_p \propto d_p^3$ for $d_p > G$ and $t_p \propto d_p^4$ for $d_p < G$. The additional one power of d_p dependence in t_p for $d_p < G$ as compared to that for $d_p > G$ is due to the fact that the number of diffusion channels is independent of d_p/G for $d_p < G$ and is proportional to d_p/G for $d_p > G$. The pore elimination time t_p has one additional power of d_p dependence in the sample-size-scaled simulations as compared to the sample-size-fixed simulations, indicating that t_p is proportional to the sample size. We explained these scaling relationships with a scaling analysis and further showed that the scaling relationships among t_p, d_p, and G should be independent of dimensionality. Therefore, the result of the present simulations should also hold for three dimensions.

The transport of matter (or vacancies) in the present simulations is mainly through grain boundaries due to the fine grain structures considered. In order to compare the results of the present simulations with experiments, the experimental systems must also have fine grains. Although the diffusion coefficient of vacancies is higher along grain boundaries, the cross-section area of grain boundaries may not be comparable to that of grains with large grains. As the ratio of the cross-section area of grain boundaries to that of the grains is increased with a decreasing grain size, the total current through grain boundaries may become larger than that through the grains.

The following is an estimate of the largest grain size of an experimental system for comparing with the present results. Let us assume that the chemical potential gradient at the grain boundaries is the same as that in the grains. For pores larger than the grains, the current through the grain boundaries J_{gb} is proportional to $D_{gb}w_{gb}$ and that through the grains J_g is proportional $D_g G$ where D_{gb}, D_g are the diffusion coefficient in the grain boundaries and that in the grains, respectively. When the ratio $J_{gb}/J_g = (D_{gb}w_{gb})/(D_g G)$ is larger than unity, grain-boundary diffusion becomes more important than lattice diffusion. The largest grain size G_c below which grain boundary diffusion is important is thus given by

$$G_c = D_{gb}w_{gb}/D_g. \qquad (37)$$

The value for G_c will depend on the material. For example, given the width of a grain boundary about 5 Å, if the ratio of the diffusion coefficient along the grain boundaries to that of grains is 10^4, G_c will be 5 μm.

Finally, it is worth mentioning that a similar scaling crossover has also been observed in the neck growth between two nanometer-sized gold particles[16] and in simulations of neck growth between two particles.[17]

ACKNOWLEDGMENTS

REFERENCES

1. For example, see I. A. Aksay, W. Y. Shih, and M. Sarikaya, in *Ultrastructure Processing of Advanced Ceramics*, edited by J. D. Mackenzie and D. R. Ulrich (John Wiley & Sons, New York, 1988), p. 393.
2. E. B. Slamovich and F. F. Lange, J. Am. Ceram. Soc. **73**, 3368–3375 (1990).
3. R. L. Coble, J. Appl. Phys. **32**, 787 (1961).
4. W. D. Kingery and B. Francois, in *Sintering and Related Phenomena*, edited by G. C. Kuczynski, N. A. Hooton, and C. F. Gibbon (Gordon and Breach, New York, 1967), pp. 471–496.
5. M. P. Anderson, D. J. Srolovitz, G. S. Grest, and P. S. Sahni, Acta Metall. **32**, 783 (1984).
6. J. E. Burke, J. Am. Ceram. Soc. **40**, 80 (1957).
7. G. N. Hassold, I-W. Chen, and D. J. Srolovitz, J. Am. Ceram. Soc. **73**, 2857 (1990); I. W. Chen, G. N. Hassold, and D. J. Srolovitz, J. Am. Ceram. Soc. **73**, 2865 (1990).
8. C. Herring, J. Appl. Phys. **21**, 301 (1950).
9. M. Schick and W-H. Shih, Phys. Rev. B **35**, 5030 (1987).
10. *Application of the Monte Carlo Method in Statistical Physics*, edited by K. Binder (Springer-Verlag, 1987).
11. F. Y. Wu, Review of Modern Physics **54**, 235 (1982).
12. J. Zhao and M. P. Harmer, J. Am. Ceram. Soc. **71**, 530 (1988).
13. E. B. Slamovich and F. F. Lange, J. Am. Ceram. Soc. **75**, 2498–2508 (1992).
14. J. Rodel and A. M. Glaeser, J. Am. Ceram. Soc. **73**, 3302 (1990).
15. For example, see p. 219 in L. H. Van Vlack, *Elements of Materials Science and Engineering*, 6th ed., Addison-Wesley, 1989.
16. J. Liu, M. Sarikaya, W. Y. Shih, and I. A. Aksay, unpublished.
17. W. Y. Shih, W-H. Shih, and I. A. Aksay, unpublished.